Available online at www.sciencedirect.com

ScienceDirect

Ceramics International 39 (2013) 8729–8736

CERAMICS INTERNATIONAL

www.elsevier.com/locate/ceramint

Effects of annealing temperature on the microstructure, optical, ferroelectric and photovoltaic properties of $BiFeO_3$ thin films prepared by sol–gel method

Zebin Lin[a], Wei Cai[a,*], Weihai Jiang[a], Chunlin Fu[a,b], Chun Li[c], Yunxia Song[a]

[a]School of Metallurgical and Materials Engineering, Chongqing University of Science and Technology, Huxi Town, Shapingba, Chongqing 401331, China
[b]State Key Laboratory of Electronic Thin Films and Integrated Devices, Chengdu 610054, China
[c]Chemical Engineering Institute, China University of Petroleum, Qingdao 266555, China

Received 19 March 2013; received in revised form 15 April 2013; accepted 16 April 2013
Available online 21 April 2013

Abstract

Bismuth ferrite thin films were prepared via sol–gel spin-coating method and the effects of annealing temperature on microstructure, optical, ferroelectric and photovoltaic properties have been investigated. The results show that the bismuth ferrite thin films annealed at 550 °C is single phase and the grain size increases with the rise of annealing temperature. The band gap of bismuth ferrite thin films annealed at 550–650 °C is between 2.306 eV and 2.453 eV. With the rise of the annealing temperature, the remnant polarization gradually decreases and the coercive electric field increases. The short circuit photocurrent density decreases with the rise of annealing temperature, and the open circuit photovoltage and the power conversion efficiency of bismuth ferrite thin films annealed at 550 °C are higher than the thin films annealed at higher temperature.

Keywords: A. Annealing temperature; C. Ferroelectric properties; C. Photovoltaic; D. Bismuth ferrite

1. Introduction

Over the past decades, many efforts have been made to develop renewable energy and clean fuel sources. In particular, solar energy has drawn great attention, in particular harvesting light energy through photovoltaic (PV) effect. Photovoltaic effect mainly involves three basic processes: (1) the generation of electron-hole pairs under illumination, (2) the separation of the electrons and holes, and (3) the movement of the electrons and holes. The charge separation in photovoltaic effect typically results from the following four mechanisms: (1) the poorly controlled granular interface [1], (2) the inherent non-centrosymmetry of bulk material [2], (3) the p–n junction or heterojunction (such as Schottky barrier) as in silicon-based solar cells [3,4], and (4) the built-in electric field caused by ferroelectricity or the domain walls [5,6]. It is noticeable that the ferroelectric thin films have a built-in electric field originating from polarization. Thus, PV effect in ferroelectric materials can be realized without p–n junction or Schottky barrier. The PV effect of ferroelectric materials, such as $BaTiO_3$ [7], $Pb(Zr,Ti)O_3$ [8–14], $(K_{0.5}Na_{0.5})(Mn_{0.005}Nb_{0.995})O_3$ [15,16], $(Bi_{3.7}Nd_{0.3})Ti_3O_{12}$ [17] and $BiFeO_3$ [18–24] has become a hot spot because of its potential applications for the photovoltaic and optoelectronic devices. Among these ferroelectric materials, $BiFeO_3$ (short for BFO) has the vast application prospect due to lead free, large spontaneous polarization, the photovoltaic characteristics controlled by electric or magnetic field and the relatively narrower band gap [25,26]. Furthermore, BFO is the only single-phase multiferroic material at room temperature because of its ferroelectric Curie temperature (~1120 K) and antiferromagnetic Neel temperature (~640 K) above room temperature [27,28]. BFO thin films can be prepared by pulsed laser deposition (PLD) [29,30], sol–gel method [31,32], molecular beam epitaxy [33], chemical vapor deposition [34] and RF magnetron sputtering [35,36]. The sol–gel method is low cost and simple for preparation of BFO thin films. Although there are a few studies about the electric properties of BFO thin films prepared by the sol–gel method, the effects of annealing temperature on photovoltaic properties of BFO thin films have not been systematically studied. We prepared the BFO thin films by the sol–gel method and studied the effects of

*Corresponding author. Tel.: +86 23 65023479; fax: +86 23 65023706.
E-mail addresses: caiwei_cqu@163.com, caiwei_cqu@yahoo.com.cn (W. Cai).

0272-8842/$ - see front matter © 2013 Elsevier Ltd and Techna Group S.r.l. All rights reserved.
http://dx.doi.org/10.1016/j.ceramint.2013.04.058

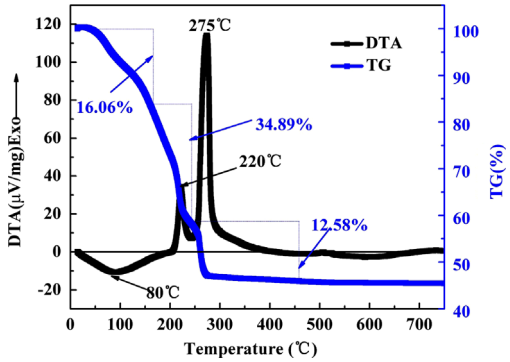

Fig. 1. DTA–TG curves of BFO gels.

annealing temperature on microstructure, optical, ferroelectric and photovoltaic properties and found out the best annealing temperature.

2. Experimental

2.1. Films preparation

BFO thin films were prepared by sol–gel method. Bismuth nitrate ($[Bi(NO_3)_3 \cdot 5H_2O]$, ≥99.0%, Sinopharm Group Co. Ltd.) and iron nitrate ($[Fe(NO_3)_3 \cdot 9H_2O]$, ≥99.0%, Sinopharm Group Co. Ltd.) were used as raw materials. At the same time, acetic acid (CH_3COOH, short for HAc, ≥99.0%, Sinopharm Group Co. Ltd.) and 2-methoxyethanol (CH_3OCH_2OH, ≥99.0%, Sinopharm Group Co. Ltd.) were used as solvent and stabilizer, respectively. Firstly, $Fe(NO_3)_3 \cdot 9H_2O$ was dissolved in the mixed solvent of CH_3OCH_2OH and HAc (the volume ratio of CH_3OCH_2OH to HAc was 4:1) to form Fe precursor solution. The solution was continuously stirred at 50 °C for 30 min to make sure Fe $(NO_3)_3 \cdot 9H_2O$ was completely dissolved. Then, Acetylacetone ($[CH_3COCH_2COCH_3]$, ≥99.0%, Sinopharm Group Co. Ltd.) was added to control the hydrolysis rate of $Fe(NO_3)_3 \cdot 9H_2O$. Dehydration of $Fe(NO_3)_3 \cdot 9H_2O$ was realized by adding acetic anhydride ($(CH_3CO)_2O$, ≥99.0%, Chengdu Kelong Chemical Reagent Factory) to obtain a clear and homogenous solution. In the similar way, Bi precursor solution was prepared. Secondly, Fe precursor solution was added to Bi precursor solution by dropping in a molar ration of Fe: Bi=1:1.05 (5 mol% excess Bi) to form the mixture, which was then stirred for 30 min at 25 °C. Then, ethanolamine ($[HOCH_2CHNH_2]$, ≥99.0%, Chengdu Kelong Chemical Reagent Factory) was added to adjust the viscosity and pH of the solution. The concentration of the precursor was adjusted to 0.2 mol/L by adding proper amount of the mixed solvent. The obtained precursor solution was transparent and homogeneous. After aging the precursor solution for 24 h at 25 °C, the thin films were deposited on the quartz glass and Pt(100 nm)/Ti(30 nm)/SiO_2(500 nm)/Si(500 μm) substrates by spin-coating method, respectively. Then, BFO thin films were annealed at 550–650 °C for 10 min in oxygen atmosphere. The thickness of BFO thin films was controlled by repeating the spin coating and heat treatments.

2.2. Characterization

To find out appropriate annealing temperature for BFO thin films, thermal analysis of the xerogel was performed based on a thermoanalyzer (DTA–TG, JCR-2, Henven, China) in the temperature range from 0 to 750 °C at a heating rate of 10 °C/min. Al_2O_3 was used as reference material and sample holders. The phase analysis was carried out at room temperature by X-ray diffraction (DX-2700 model, Dandong Fangyuan, China, Cu target with a working voltage of 30 kV and a current of 20 mA) in a scanning rate of 3°/min. Surface morphology was determined by scanning electron microscope (S-3700N model, Hitachi, Tokyo, Japan). The thickness of BFO thin films is about 240 nm determined by step profiler (Dekatk 150, Veeco, USA). The optical transmission characteristics were studied by a double beam ultraviolet–visible (UV–vis) spectrophotometer (TU1810, Persee, China) in the wavelength range of 200–1100 nm. To measure the photovoltaic characteristic and electric properties, the Au top electrodes of 200 μm in a diameter were deposited on the BFO thin films using DC magnetron sputtering (JGP280, SKY, China). The ferroelectric and leakage measurements were made by ferroelectric test system (TF2000e, aixACCT, Germany). The current–voltage (*I–V*) behavior was characterized by a current source meter (2400, Keithley, USA) when the thin films were illuminated with the solar simulator (Newport, Oriel instrument, USA).

3. Results and discussion

3.1. Annealing temperature

Fig. 1 shows DTA–TG curves of BFO gels. Firstly, one endothermic reaction occurs near 80 °C due to dehydration of residual water and removal of organic solvents, leading to a weight loss around 16.06%. Secondly, there are two obvious exothermic peaks near 220 °C and 275 °C, respectively. Between 180 °C and 400 °C, the significant weight loss around 47.47% (34.89%+12.58%) corresponds to pyrolysis of organic residues. Thirdly, there is a small endothermic peak near 593 °C and the weight is unchanged, which implies that there is crystallization of BFO thin films. Therefore, the annealing temperature of BFO thin films is set as 550 °C, 600 °C and 650 °C, respectively. The effects of annealing temperature on microstructure, optical, ferroelectric and photovoltaic properties of BFO thin films have been investigated.

3.2. Microstructure

Fig. 2 shows the XRD patterns of BFO thin films annealed at different temperatures. Firstly, it is found that the main diffraction peaks in samples annealed at 550–650 °C are indexed as a rhombohedral distortion perovskite structure ($BiFeO_3$, *R3m* space group, JCPDS card no. 73–2548). No secondary phase is observed in the sample annealed at 550 °C. But there is secondary phase identified as $Bi_2Fe_4O_9$ (JCPDS card no. 74-1098 marked with # in Fig. 2) in the samples

annealed at 600 °C and 650 °C, which is commonly observed in this system [24,25]. It is worthwhile to note that the intensity of diffraction peaks corresponding to the secondary phase becomes stronger with the rise of annealing temperature. The content of $Bi_2Fe_4O_9$ in the sample annealed at 650 °C reaches 34.26 wt% by means of XRD quantitative analysis. The emergence of secondary phase $Bi_2Fe_4O_9$ is attributed to that the kinetics of phase formation because of the volatilization of some reactants and phase decompositions at high temperature [37].

The grain size of BFO thin films was determined by Scherer's formula:

$$d = \frac{K\lambda}{\beta \cos\ \theta} \tag{1}$$

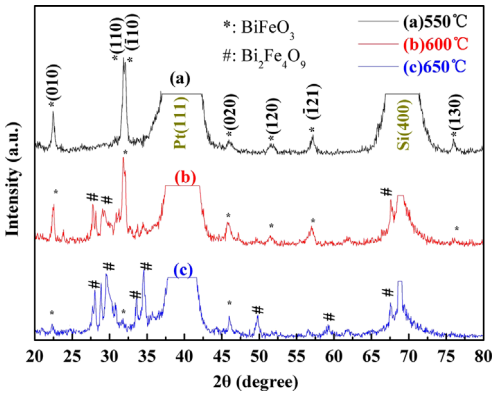

Fig. 2. XRD patterns of BFO thin films annealed at different temperatures.

where d is the grain size (nm), K is the Scherrer constant (0.89), λ is the wavelength of X-rays (0.15406 nm), β is the full width at half maximum reflection height and θ is the diffraction angle. Based on Eq. (1), the grain size of BFO thin film annealed at 550 °C, 600 °C and 650 °C is 20 nm, 22 nm and 29 nm, respectively. It indicates that the grain size increases with the rise of annealing temperature.

Fig. 3 shows SEM micrographs of BFO thin films annealed at different temperatures. Firstly, it is found that the BFO thin films annealed at 550–650 °C are crack-free, homogeneous and dense. The BFO thin films annealed at 650 °C is denser than that annealed at 550 °C and 600 °C. It may be due to the higher crystallinity in the sample annealed at 650 °C. Secondly, the grain size increases with the rise of annealing temperature. In particular, the grain size of the sample annealed at 650 °C is obviously larger than that annealed at 550 °C and 600 °C, which is consistent with the calculated results according to the Scherrer formula. Moreover, there are some obvious white particulates in the sample annealed at 650 °C. According to the XRD patterns, it is inferred that the white particulates is secondary phase $Bi_2Fe_4O_9$.

3.3. Optical properties

Fig. 4(a) shows the optical transmission spectra and absorption spectra of BFO thin films annealed at different temperatures. The absorption coefficient α is deduced by the formula:

$$\alpha = 1/t\ \ln(1/T) \tag{2}$$

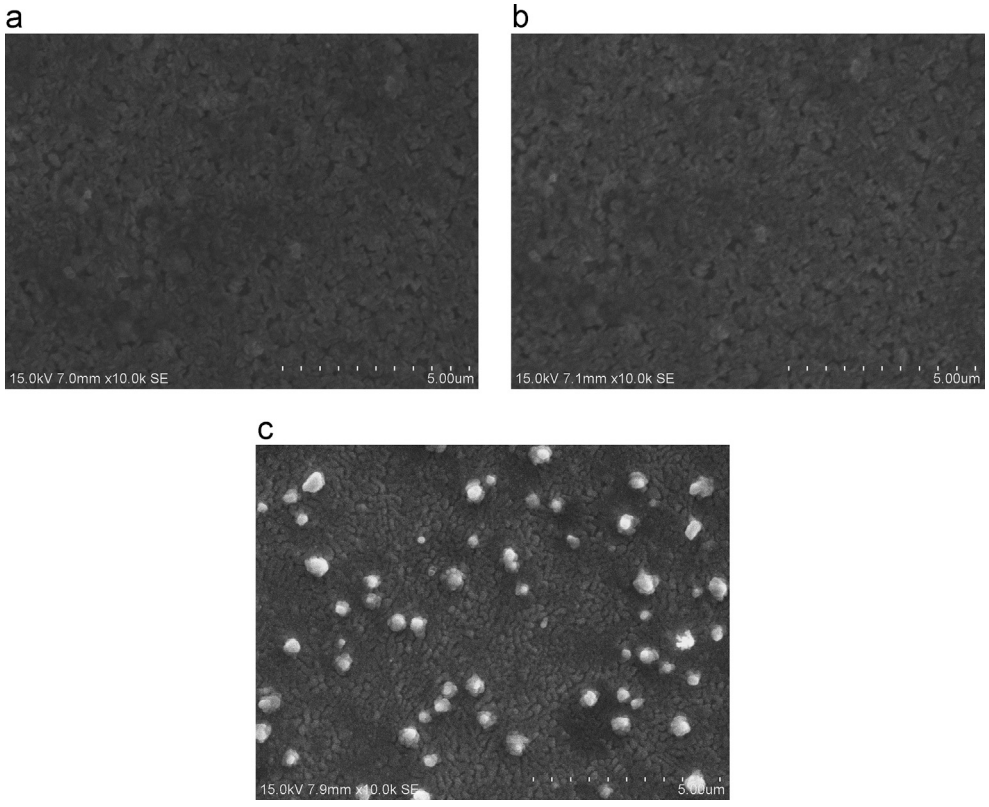

Fig. 3. SEM micrographs of BFO thin films annealed at different temperatures (a) 550 °C, (b) 600 °C, and (c)650 °C.

where t means the thickness of the film (t of BFO thin films has been determined by step profiler) and T represents the transmittance. The region of the absorption edge shows that the fundamental absorption edge for these samples is around 1.62 eV (corresponding to 766 nm), which means the BFO thin films can absorb visible light, while typical ferroelectric materials such as $BaTiO_3$-based thin films only has a good absorption of ultraviolet light because of its wide band gap (>3 eV) [38]. Although the overall absorption profiles for BFO thin films annealed at 550–650 °C are similar, there are some differences in the higher absorption region (energy is between 2.5 eV and 6.25 eV). The absorption coefficient α of the sample annealed at 650 °C is obviously lower than that annealed at 550 °C and 600 °C. It may be caused by the impurity phase resulting from the higher annealing temperature. The result of transmission spectra is in agreement with that of absorption spectra.

The optical band gap of BFO thin films was calculated via Tauc's Law

$$(\alpha h\nu)^n = A(h\nu - E_g) \quad (3)$$

where A is a constant, α is the absorption coefficient, $h\nu$ is the photon energy, n represents the type of optical transition between valence and conduction bands, E_g is the optical band gap. For $n=2$, the transition is direct, while $n=0.5$ indicates an indirect optical transition [39]. However, there is the dispute about n value of BFO thin films. Ihlefeld et al. [40] et al. found that the BFO thin films is direct band gap semiconductor, n is 2. But some researchers contend that the BFO thin films is indirect band gap semiconductor, n is 0.5 [41,42]. To solve the problem, the curves were obtained by plotting $(\alpha h\nu)^2$ and versus $h\nu$, $(\alpha h\nu)^{0.5}$ and versus $h\nu$, respectively (shown in the inner figure of Fig. 4(b)). In our data, the lack of the characteristic shape of the $(\alpha h\nu)^{0.5}$ versus $h\nu$ plot indicates the required phonon participation argues against an indirect gap. Therefore, E_g can be obtained by plotting $(\alpha h\nu)^2$ versus $h\nu$ and extrapolating the linear portion of the plot to $(\alpha h\nu)^2=0$ (shown in Fig. 4(b)). The band gap values of the samples annealed at different temperatures are listed in the table of Fig. 4(b). These values are similar to Ihlefeld's result [40]. The band gap of the samples is between 2.306 eV and 2.453 eV, which indicates that the BFO thin films can absorb visible light. The band gap of BFO thin films annealed at 600 °C and 650 °C is lower than that of BFO thin films annealed at 550 °C, which may be attributed to the improvement of crystallinity. The result is consistent with the Sharma's results [43,44]. But it is important to note that the band gap of BFO thin films annealed at 650 °C is slightly higher than that of the sample annealed at 600 °C. It may be due to the greater proportion of secondary phase $Bi_2Fe_4O_9$ in the sample annealed at 650 °C.

3.4. Ferroelectric properties

Fig. 5 shows the room temperature hysteresis loops of BFO thin films annealed at different temperatures measured at 200 Hz. Firstly, it is found that BFO thin films exhibit typical

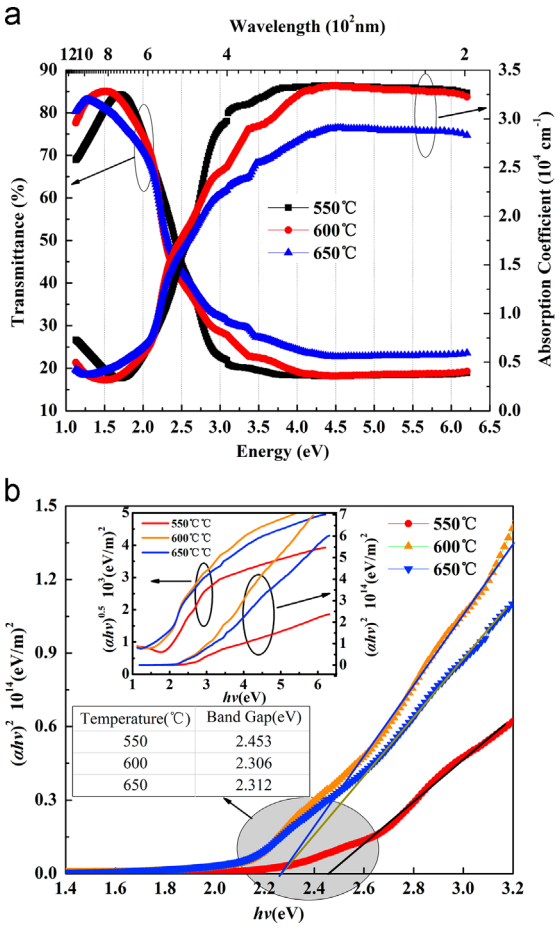

Fig. 4. (a) Transmission and absorption spectra and (b) dependence of $(\alpha h\nu)^2$ on $h\nu$ of BFO thin films anealed at different temperatures.

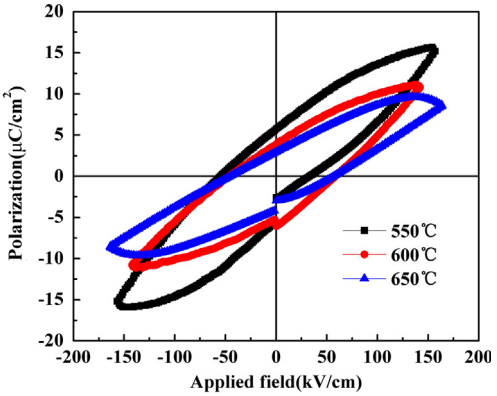

Fig. 5. Room temperature hysteresis loops of BFO thin film annealed at different temperatures.

hysteresis loops. The remnant polarization (P_r) and coercive electric field (E_C) of the samples annealed at different temperatures are shown in Table 1. As the annealing temperature rises, the remnant polarization gradually decreases and the coercive electric field increases. The change of the remnant polarization is due to two reasons. On the one hand, the secondary phase $Bi_2Fe_4O_9$, whose Curie temperature is −23 °C [45], in BFO thin films annealed at higher temperature is

Table 1
The remnant polarization and coercive electric field of BFO thin films annealed at different temperatures.

Annealing temperature (°C)	550	600	650
$2P_r$ (μC/cm^2)	11.44	7.74	5.91
$2E_c$ (kV/cm)	86.3	105.1	105.1

paraelectric phase at room temperature. It results in the decrease of remnant polarization. On the other hand, the higher oxygen vacancy concentrations result from more Fe^{2+} ions in the sample at higher annealing temperatures [28]. Oxygen vacancies act as space charge, which causes strong domain pinning. The higher annealing temperature leads to more oxygen vacancies. The increase of defect concentration results in the decrease in the remnant polarization [46]. In this manner, the remnant polarization of BFO thin films decreases with the rise of annealing temperature. Moreover, the increase of the coercive electric field in the sample annealed at higher temperature may be determined by the competition of the higher oxygen vacancy concentration and the larger grain size. On the one hand, oxygen vacancy may affect domain wall motion by screening of the polarization charge. A formation of mechanical barriers against the domain walls by oxygen vacancies, so called domain wall pinning, might also stabilize the domain configuration [47]. As mentioned above, high annealing temperature leads to the increase of oxygen vacancy concentration. It indicates that as annealing temperature rises, domain wall pinning enhances so that domain wall moves difficultly so as to increase the coercive electric field. On the other hand, barrier for switching ferroelectric domain must be broken through and energy barrier decreases as grain size increases. So the reversal polarization of a ferroelectric domain in a small grain is more difficult than that in a large grain [48]. As mentioned above, the grain size of BFO thin films increases with the rise of annealing temperature and leads to the decrease of coercive electric field. But in two opposite effects, the increase of oxygen vacancy concentration caused by higher annealing temperature is dominant, so the coercive electric field increases.

Fig. 6 shows DC leakage characteristic of BFO thin film annealed at different temperatures measured at 200 Hz and room temperature. It is found that the leakage current of BFO thin films is very sensitive to the annealing temperature, i.e. the higher the annealing temperature, the greater the leakage current. A similar dependence of leakage current on annealing temperature has been reported in BFO, La-doped BFO, Ce-doped BFO and Mn-doped BFO thin films [49–52]. The leakage behavior in BFO thin films depends on phase purity, grain size, defects such as oxygen vacancy, and so on. Among all the factors, oxygen vacancy may play an important role. Oxygen vacancies generate according to the reaction:

$$O_o^x \rightarrow V_o^{\cdot\cdot} + 2e' + \frac{1}{2}O_2\uparrow \quad (4)$$

alternatively, reduction of Fe^{3+} to Fe^{2+} can be ruled out to compensate the space charges according to the reaction:

$$O_o + 2Fe_{Fe} \rightarrow \frac{1}{2}O_2\uparrow + V_o^{\cdot\cdot} + 2Fe'_{Fe} \quad (5)$$

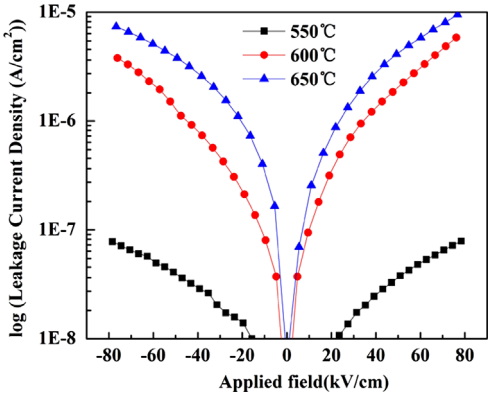

Fig. 6. DC leakage of BFO thin film annealed at different temperatures.

The oxygen vacancies formed during growth cause a portion of the Fe^{3+} ions to become Fe^{2+}. These Fe ions are responsible for the high leakage of BFO. The higher annealing temperature leads to the more oxygen vacancies, which causes the higher leakage [53,54].

3.5. Photovoltaic characteristic

Fig. 7 shows illuminated *J–V* curves and the terminal voltage dependences of power conversion efficiency for BFO thin films annealed at different temperatures. Firstly, it can be seen that the short circuit photocurrent density (the intercept of *J*-axis and *J–V* curve, short for J_{SC}) and the open circuit photovoltage (the intercept of *V*-axis and *J–V* curve, short for V_{OC}) are negative. This is due to the different work functions between BFO thin films and the electrodes [55]. Secondly, the short circuit photocurrent density and open circuit photovoltage of BFO thin films are shown in Table 2. It is found that the short circuit photocurrent density decreases with the rise of annealing temperature, and the open circuit photovoltage of the sample annealed at 550 °C is higher than that of the samples annealed at higher temperature. It is well known that the J_{SC} and V_{OC} of ferroelectric thin films under illumination depend heavily on the built-in electric field caused by the remnant polarization. As mentioned above, the remnant polarization of BFO thin films decreases with the rise of annealing temperature. Therefore, the higher photovoltaic output in BFO thin films annealed at 550 °C is due to its higher internal depolarization field caused by the larger remnant polarization. The result is similar to Qin's [55] and Zheng's [56] results. It is believed that the larger depolarization field could separate the electron and holes more effectively and enhance the photovoltaic output of BFO thin films. Thirdly, the light-to-electricity power conversion efficiency η can be determined from the illuminated *J–V* curves (shown in Fig. 7(b)). The input power density P_{in} (mW/cm^2) is the simulated solar light intensity I_{so} (mW/cm^2), and the photovoltaic output power density is $P_{out}=JV$ (mW/cm^2). The power conversion efficiency η at the point (*J*, *V*) can be calculated as:

$$\eta = \frac{P_{out}}{P_{in}} = \frac{P_{out}}{I_{so}} = \frac{JV}{I_{so}} \quad (6)$$

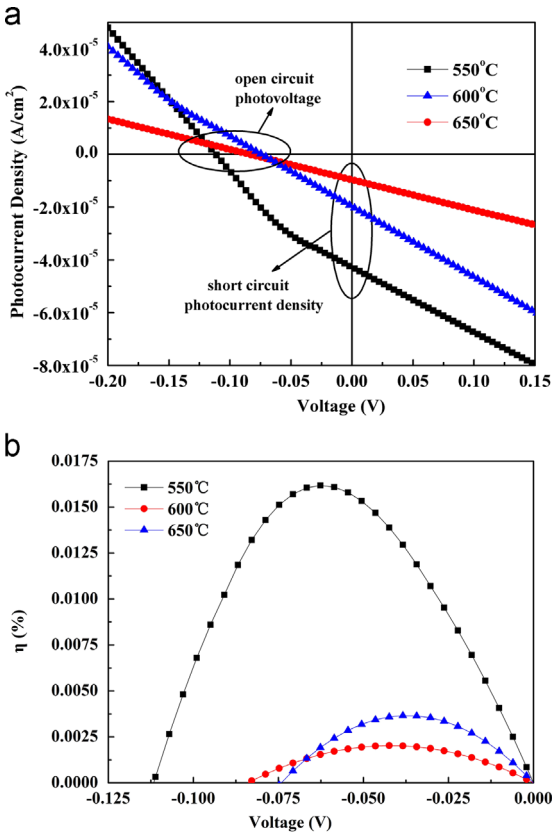

Fig. 7. (a) Illuminated *J–V* curves and (b) corresponding terminal voltage dependence of light-to-electricity power conversion efficiency for BFO thin films annealed at different temperatures.

Table 2
The short circuit photocurrent density and the open circuit photovoltage of BFO thin films annealed at different temperatures.

Annealing temperature (°C)	550	600	650
J_{SC} (10^{-5} A/cm^2)	4.327	2.031	0.990
V_{OC} (V)	0.11	0.075	0.078

based on the illuminated *J–V* curve, the voltage dependence of power conversion efficiency of BFO thin films is presented in Fig. 7(b). It can be found that the maximum power conversion efficiency η_{max} of the samples annealed at 550–650 °C occurs at about half of the open circuit photovoltage. The η_{max} of BFO thin films annealed at 550 °C, 600 °C and 650 °C is 0.01617%, 0.00203%, and 0.00366%, respectively. The power conversion efficiency is related to the separation and movement of carriers driven by the polarization. The higher remnant polarization of the samples annealed at 550 °C provides the larger electric field as driving force to separate the light electron-hole carriers and leads to higher power conversion efficiency. But it is worthwhile to note that although the remnant polarization of BFO thin films annealed at 600 °C is higher than that of the sample annealed at 650 °C, the power conversion efficiency of thin films annealed at 600 °C is lower than that of the sample annealed at 650 °C. It may be related to more secondary phase in BFO thin films annealed at 650 °C. This problem will be further studied. The power conversion efficiency of BFO is higher than that of wide band gap PZT-based thin films [57], but is lower than that of epitaxial BFO thin films [58]. Moreover, the power conversion efficiency of Au/BFO/Pt structure in our paper is lower than that of ITO/BFO/Pt, which can absorb more visble light [59]. In summary, the single-phase BFO thin films annealed at 550 °C has narrow band gap, relatively lower leakage current, larger remnant polarization, lower coercive electric field, larger photovoltaic output and light-to-electricity power conversion efficiency. Therefore, 550 °C for BFO thin films prepared by sol–gel method is the best annealing temperature.

4. Conclusions

BFO thin films were prepared by sol–gel method and the effects of annealing temperature on microstructure, optical, ferroelectric and photovoltaic properties have been investigated. The BFO thin films annealed at 550 °C is single phase and the higher annealing temperature leads to the existence of secondary phase $Bi_2Fe_4O_9$. The grain size increases with the rise of annealing temperature. BFO thin films annealed at 550–650 °C can absorb visible light because of its narrow band gap (2.306–2.453 eV). As the annealing temperature rises, the remnant polarization gradually decreases and the coercive electric field increases. The short circuit photocurrent density of BFO thin films decreases with the rise of annealing temperature, and the open circuit photovoltage and power conversion efficiency of BFO thin films annealed at 550 °C is higher than that of the sample annealed at higher temperature. It results from the change of remnant polarization.

Acknowledgment

This work was supported by the National Natural Science Foundation of China (51102288), Natural Science Foundation of Chongqing, China (CSTC2011BA4027), Open Research Fund of State Key Laboratory of Electronic Thin Films and Integrated Devices (UESTC) (KFJJ201104) and Research Foundation of Chongqing University of Science and Technology (CK2013B08).

References

[1] P.S. Brody, F. Crowne, Mechanism for the high voltage photovoltaic effect in ceramic ferroelectrics, Journal of Electronic Materials 4 (1975) 955–971.
[2] M. Ichiki, H. Furue, T. Kobayashi, R. Maeda, Y. Morikawa, T. Nakada, K. Nonaka, Photovoltaic properties of (Pb,La)(Zr,Ti)O_3 films with different crystallographic orientations, Applied Physics Letters 87 (2005) 222903.
[3] D. Li, L. Wang, D.S. Li, N. Zhou, Z.Q. Feng, X.P. Zhong, D.R. Yang, Formation of nanostructured emitter for silicon solar cells using catalytic silver nanoparticles, Applied Surface Science 264 (2013) 621–624.
[4] D.Z. Dimitrov, C.H. Du, Crystalline silicon solar cells with micro/nano texture, Applied Surface Science 266 (2013) 1–4.
[5] S.Y. Yang, J. Seidel, S.J. Byrnes, P. Shafer, C.H. Yang, M.D. Rossell, P. Yu, Y.H. Chu, J.F. Scott, J.W. Ager III, L.W. Martin, R. Ramesh,

Above-band gap voltages from ferroelectric photovoltaic devices, Nature Nanotechnology 5 (2010) 143–147.
[6] J. Seidel, D.Y. Fu, S.Y. Yang, E.A. Lladó, J.Q. Wu, R. Ramesh, J.W. Ager III, Efficient photovoltaic current generation at ferroelectric domain walls, Physical Review Letters 107 (2011) 126805.
[7] C.J. Won, Y.A. Park, K.D. Lee, H.Y. Ryu, N. Hur, Diode and photocurrent effect in ferroelectric $BaTiO_{3-\delta}$, Journal of Applied Physics 109 (2011) 084108.
[8] P. Zhang, D.W. Cao, C.Y. Wang, M.R. Shen, X.D. Su, L. Fang, W. Dong, F.G. Zheng, Enhanced photocurrent in $Pb(Zr_{0.2}Ti_{0.8})O_3$ ferroelectric film by artificially introducing asymmetrical interface Schottky barriers, Materials Chemistry and Physics 135 (2012) 304–308.
[9] V.N. Harshan, S. Kotru, Influence of work-function of top electrodes on the photovoltaic characteristics of $Pb_{0.95}La_{0.05}Zr_{0.54}Ti_{0.46}O_3$ thin film capacitors, Applied Physics Letters 100 (2012) 173901.
[10] B. Chen, Z.H. Zuo, Y.W. Liu, Q.F. Zhan, Y.L. Xie, H.L. Yang, G.H. Dai, Z.X. Li, G.J. Xu, R.W. Li, Tunable photovoltaic effects in transparent $Pb(Zr_{0.53},Ti_{0.47})O_3$ capacitors, Applied Physics Letters 100 (2012) 173903.
[11] L. Pintilie, C. Dragoi, I. Pintilie, Interface controlled photovoltaic effect in epitaxial $Pb(Zr,Ti)O_3$ films with tetragonal structure, Journal of Applied Physics 110 (2011) 044105.
[12] D.W. Cao, C.Y. Wang, F.G. Zheng, W. Dong, L. Fang, M.R. Shen, High-efficiency ferroelectric-film solar cells with an n-type Cu_2O cathode buffer layer, Nano Letters 12 (2012) 2803–2809.
[13] D.W. Cao, C.Y. Wang, F.G. Zheng, L. Fang, W. Dong, M.R. Shen, Understanding the nature of remnant polarization enhancement, coercive voltage offset and time-dependent photocurrent in ferroelectric films irradiated by ultraviolet light, Journal of Materials Chemistry 22 (2012) 12592–12598.
[14] X.L. Yang, X.D. Su, M.R. Shen, F.G. Zheng, Y. Xin, L. Zhang, M.C. Hua, Y.J. Chen, V.G. Harris, Enhancement of photocurrent in ferroelectric films via the incorporation of narrow bandgap nanoparticles, Advanced Materials 24 (2012) 1202–1208.
[15] J.M. Park, C.Won Ahn, Won Kim III, Photocurrent of lead-free $(K_{0.5}Na_{0.5})(Mn_{0.005}Nb_{0.995})O_3$ ferroelectric nanotubes, Journal of Applied Physics 112 (2012) 014312.
[16] J.M. Park, C.Won Ahn, Won Kim III, Ferroelectric photocurrent effect in polycrystalline lead-free $(K_{0.5}Na_{0.5})(Mn_{0.005}Nb_{0.995})O_3$ thin film, Journal of the American Ceramic Society 96 (2013) 146–150.
[17] D.W. Cao, H. Zhang, L. Fang, W. Dong, F.G. Zheng, M.R. Shen, Polarization effect on the photocurrent of Pt sandwiched multi-crystalline ferroelectric films, Materials Chemistry and Physics 129 (2011) 783–786.
[18] G. Gopal Khan, R. Das, N. Mukherjee, K. Mandal, Effect of metal doping on highly efficient photovoltaics and switchable photovoltage in bismuth ferrite nanotubes, Physica Status Solidi (RRL)—Rapid Research Letters 6 (2012) 312–314.
[19] W. Dong, Y.P. Guo, B. Guo, H.Y. Liu, H. Li, H.Z. Liu, Photovoltaic properties of $BiFeO_3$ thin film capacitors by using Al-doped zinc oxide as top electrode, Materials Letters 91 (2013) 359–361.
[20] R. Moubah, O. Rousseau, D. Colson, A. Artemenko, M. Maglione, M. Viret, Photoelectric effects in single domain $BiFeO_3$ crystals, Advanced Functional Materials 22 (2012) 4814–4818.
[21] Y.Y. Zang, D. Xie, Y. Chen, X. Wu, T.L. Ren, H.W. Zhu, J.L. Cao, D. Plant, Investigation of the improved performance in a graphene/polycrystalline $BiFeO_3$/Pt photovoltaic heterojunction: Experiment, modeling, and application, Journal of Applied Physics, 112, 054103.
[22] R. Guo, L. You, L. Chen, D. Wu, J.L. Wang, Photovoltaic property of $BiFeO_3$ thin films with 109° domains, Applied Physics Letters 99 (2011) 122902.
[23] Y.Y. Zang, D. Xie, Y. Chen, X. Wu, T.L. Ren, J.Q. Wei, H.W. Zhu, D. Plant, Electrical and thermal properties of a carbon nanotube/polycrystalline $BiFeO_3$/Pt photovoltaic heterojunction with CdSe quantum dots sensitization, Nanoscale 4 (2012) 2926–2930.
[24] F. Yan, G.N. Chen, L. Lu, J.E. Spanier, Dynamics of photogenerated surface charge on $BiFeO_3$ films, ACS Nano 6 (2012) 2353–2360.
[25] Y.X. Sun, X.Y. Xiong, Z. Xia, H.R. Liu, Y. Zhou, M. Luo, C.Y. Wang, Study on visible light response and magnetism of bismuth ferrites synthesized by a low temperature hydrothermal method, Ceramics International 39 (2013) 4651–4656.
[26] G. Catalan, J.F. Scott, Physics and applications of bismuth ferrite, Advanced Materials 21 (2009) 2463–2485.
[27] Y. Ukai, S. Yamazaki, T. Kawae, A. Morimoto, Polarization-induced photovoltaic effects in Nd-doped $BiFeO_3$ ferroelectric thin films, Japanese Journal of Applied Physics 51 (2012) 09LE10.
[28] E.C. Aguiar, M.A Ramirez, F Moura, J.A Varela, E Longo, A.Z. Simões, Low-temperature synthesis of nanosized bismuth ferrite by the soft chemical method, Ceramics International 39 (2013) 13–20.
[29] P.V. Chinta, S.J. Callori, M. Dawber, A. Ashrafi, R.L. Headrick, Transition from laminar to three-dimensional growth mode in pulsed laser deposited $BiFeO_3$ film on (001) $SrTiO_3$, Applied Physics Letters 101 (2012) 201602.
[30] Y.C. Chen, G.F. Wang, H.H. Tai, J.W. Chen, Y.C. Huang, J.C. Yang, Y.H. Chu, Non-volatile domain nucleation and growth in multiferroic $BiFeO_3$ films, Nanotechnology 22 (2011) 254030.
[31] B. Chen, M. Li, Y.W. Liu, Z.H. Zuo, F. Zhuge, Q.F. Zhan, R.W. Li, Effect of top electrodes on photovoltaic properties of polycrystalline $BiFeO_3$ based thin film capacitors, Nanotechnology 22 (2011) 195201.
[32] D.H. Zhang, P. Shi, X.Q. Wu, W. Ren, Structural and electrical properties of sol–gel-derived Al-doped bismuth ferrite thin films, Ceramics International 39 (2013) S461–S464.
[33] J.F. Ihlefeld, N.J. Podraza, Z.K. Liu, R.C Rai, X. Xu, T. Heeg, Y.B. Chen, J. Li, R.W. Collins, J.L. Musfeldt, X.Q. Pan, J. Schubert, R. Ramesh, D.G. Schlom, Optical band gap of $BiFeO_3$ grown by molecular-beam epitaxy, Applied Physics Letters 92 (2008) 142908.
[34] J.X. Zhang, B. Xiang, Q. He, J. Seidel, R.J. Zeches, P. Yu, S.Y. Yang, C.H. Wang, Y.H. Chu, L.W. Martin, A.M. Minor, R. Ramesh, Large field-induced strains in a lead-free piezoelectric material, Nature Nanotechnology 6 (2011) 98–102.
[35] H.J. Lee, M.H. Park, Y.J. Kim, C.S. Hwang, J.H. Kim, H. Funakubo, H. Ishiwara, Improved ferroelectric property of very thin Mn-doped $BiFeO_3$ films by an inlaid Al_2O_3 tunnel switch, Journal of Applied Physics 110 (2011) 074111.
[36] F. Fan, B.C. Luo, M.M. Duan, H. Xing, K.X. Jin, C.L. Chen, Ferroelectric domain switching investigation of $BiFeO_3$ thin film on Pt/Ti/SiO_2/Si (111) substrate, Applied Surface Science 258 (2012) 7412–7416.
[37] M.S. Bernardo, T. Jardiel, M. Peiteado, A.C. Caballero, M. Villegas, Reaction pathways in the solid state synthesis of multiferroic $BiFeO_3$, Journal of the European Ceramic Society 31 (2011) 3047–3053.
[38] K. Venkata Saravanan, K. Sudheendran, M. Ghanashyam Krishna, K.C. James Raju, Anil K. Bhatnagar, Structural, optical and microwave characteristics of sol-gel derived barium strontium titanate thin films, Materials Chemistry and Physics 105 (2007) 426–432.
[39] W. Cai, C.L. Fu, J.C. Gao, Q. Guo, X.L. Deng, C.Y. Zhang, Preparation and optical properties of barium titanate thin films, Physica B 406 (2011) 3583–3587.
[40] J.F. Ihlefeld, N.J. Podraza, Z.K. Liu, R.C. Rai, X. Xu, T. Heeg, Y.B. Chen, J. Li, R.W. Collins, J.L. Musfeldt, X.Q. Pan, J. Schubert, R. Ramesh, D.G. Schlom, Optical band gap of $BiFeO_3$ grown by molecular-beam epitaxy, Applied Physics Letters 92 (2008) 142908.
[41] V. Fruth, E. Tenea, M. Gartner, M. Anastasescu, D. Berger, R. Ramer, M. Zaharescu, Preparation of $BiFeO_3$ films by wet chemical method and their characterization, Journal of the European Ceramic Society 27 (2007) 937–940.
[42] T.P. Gujar, V.R. Shinde, C.D. Lokhande, Nanocrystalline and highly resistive bismuth ferric oxide thin films by a simple chemical method, Materials Chemistry and Physics 103 (2007) 142–146.
[43] S.B. Singh, B.S. Ngangom, H.B. Sharma, Effect of annealing temperatures on the structural and optical properties of sol–gel processed nanocrystalline $BiFeO_3$ thin films, Thin Solid Film 524 (2012) 57–61.
[44] H.B. Sharma, S.B. Singh, N.B. Singh, Structural and optical properties of low temperature synthesized nanostructured $BiFeO_3$ thin films, Physica B 406 (2011) 351–353.
[45] A.K. Singh, S.D. Kaushik, B. Kumar, P.K. Mishra, A. Venimadhav, V. Siruguri, S. Patnaik, Substantial magnetoelectric coupling near room temperature in $Bi_2Fe_4O_9$, Applied Physics Letters 92 (2008) 132910.

[46] Y. Noguchi, I. Miwa, Y. Gosshima, M. Miyayama, Defect control for large remanent polarization in bismuth titanate ferroelectrics-doping effect of higher-valent cations-, Japanese Journal of Applied Physics 39 (2000) L11259.
[47] W. Cai, C.L. Fu, Z.B. Lin, X.L. Deng, Vanadium doping effects on microstructure and dielectric properties of barium titanate ceramics, Ceramics International 37 (2011) 3643–3650.
[48] C.C. Leu, C.Y. Chen, C.H. Chien, M.N. Chang, F.Y. Hsu, C.T. Hu, Domain structure study of $SrBi_2Ta_2O_9$ ferroelectric thin films by scanning capacitance microscopy, Applied Physics Letters 82 (2003) 3493–3495.
[49] K.B. Yin, M. Li, Y.W. Liu, C.L. He, F. Zhuge, B. Chen, W. Lu, X.Q. Pan, R.W. Li, Resistance switching in polycrystalline $BiFeO_3$ thin films, Applied Physics Letters 97 (2010) 042101.
[50] F. Gao, X.Y. Qiu, Y. Yuan, B. Xu, Y.Y. Wen, F. Yuan, L.Y. Lv, J.M. Liu, Effects of substrate temperature on $Bi_{0.8}La_{0.2}FeO_3$ thin films prepared by pulsed laser deposition, Thin Solid Films 515 (2007) 5366–5373.
[51] X.J. Zhu, F. Zhuge, M. Li, K.B. Yin, Y.W. Liu, Z.H. Zuo, B. Chen, R.W. Li, Microstructure dependence of leakage and resistive switching behaviours in Ce-doped $BiFeO_3$ thin films, Journal of Physics D: Applied Physics 44 (2011) 415104.
[52] H. Naganuma, J. Miura, S. Okamura, Annealing temperature effect on ferroelectric and magnetic properties in Mn-added polycrystalline $BiFeO_3$ films, Journal of Electroceramics 22 (2009) 203–208.
[53] G.W. Pabst, L.W. Martin, Y.H. Chu, R. Ramesh, Leakage mechanisms in $BiFeO_3$ thin films, Applied Physics Letters 90 (2007) 072902.
[54] S.K. Singh, H. Ishiwara, Micro-structure and ferroelectric properties of $BiFeO_3$ thin films formed on Pt-coated r-plane sapphire substrates, Journal of Electroceramics 16 (2006) 553–556.
[55] M. Qin, K. Yao, Y.C. Liang, Photovoltaic characteristics in polycrystalline and epitaxial $(Pb_{0.97}La_{0.03})(Zr_{0.52}Ti_{0.48})O_3$ ferroelectric thin films sandwiched between different top and bottom electrodes, Journal of Applied Physics 105 (2009) 061624.
[56] F.G. Zheng, J. Xu, L. Fang, M.R. Shen, X.L. Wu, Separation of the Schottky barrier and polarization effects on the photocurrent of Pt sandwiched $Pb(Zr_{0.20}Ti_{0.80})O_3$ films, Applied Physics Letters 93 (2008) 172101.
[57] M. Qin, K. Yao, Y.C. Liang, High efficient photovoltaics in nanoscaled ferroelectric thin films, Applied Physics Letters 93 (2008) 122904.
[58] S.Y. Yang, L.W. Martin, S.J. Byrnes, T.E. Conry, S.R. Basu, D. Paran, L. Reichertz, J. Ihlefeld, C. Adamo, A. Melville, Y.H. Chu, C.H. Yang, J.L. Musfeldt, D.G. Schlom, J.W. Ager III, R. Ramesh, Photovoltaic effects in $BiFeO_3$, Applied Physics Letters 95 (2009) 062909.
[59] W. Dong, Y.P. Guo, B. Guo, H.Y. Liu, H. Li, H.Z. Liu, Enhanced photovoltaic properties in polycrystalline $BiFeO_3$ thin films with rhombohedral perovskite structured eposited on fluorine doped tin oxide substrates, Materials Letters 88 (2012) 140–142.